

Micron-sized magnonic 3-port rectilinear circulator

Kevin S. Weber,^{1,2,3,*} Loic Temdie,^{1,2,4} Vincent Castel,^{1,2} Timmy Reimann,⁵ Morris Lindner,⁵ Carsten Dubs,⁵ Yves Henry,⁶ Matthieu Bailleul,⁶ and Vincent Vlaminck^{1,2,†}

¹*Département Micro-Ondes, Institut Mines-Télécom (IMT) Atlantique, Technopole Brest-Iroise CS83818, CEDEX 03, 29238 Brest, France*

²*Laboratoire des Sciences et Techniques de l'Information de la Communication et de la Connaissance (Lab-STICC), Unité Mixte de Recherche (UMR) 6285, CNRS, Technopole Brest-Iroise CS83818, CEDEX 03, 29238 Brest, France*

³*QZabre Ltd., Neunbrunnenstrasse 50, 8050 Zürich, Switzerland*

⁴*SPEC, CEA, CNRS, Université Paris-Saclay, CEA Saclay, 91191 Gif-sur-Yvette Cedex, France*

⁵*INNOVENT e.V. Technologieentwicklung, Pruessingstrasse 27B, 07745 Jena, Germany*

⁶*Unité Mixte de Recherche (UMR) 7504, CNRS, Institut de Physique et Chimie des Matériaux de Strasbourg, Université de Strasbourg (IPCMS), CEDEX, 67000 Strasbourg, France*

(Dated: June 12, 2026)

The development of miniaturized non-reciprocal microwave technologies compatible with integrated circuit architectures remains a critical challenge for modern information technology. Here, we present the first experimental characterization of a micron-sized prototypical magnon circulator. Taking advantage of the chiral excitation of spin-waves via nanowire gratings, we propose an original design of a circulator involving three channels of rectilinear and unidirectional spin-wave beams. We demonstrate via a full 3-port spin-wave spectroscopy a genuine spin-wave circulation between the three ports. The narrow frequency band of operation can be tuned over a broad range of frequencies (2–8 GHz) with both an external field of up to 100 mT, and the dimensions of the grating specifying the wavevectors. This proposed scheme opens up possibilities for new architectures of integrated and miniaturized non-reciprocal microwave devices.

Non-reciprocal components such as circulators and isolators are indispensable for protecting microwave systems from reflections, isolating radar signals, and shielding qubits in quantum architectures[1]. However, these functionalities are not easily achieved with standard electric-field devices. The current ferrite-based technologies relying on the gyrotropic nature of magnetization remain bulky and off-chip, which limits their miniaturization into microscale electronics. This necessitates the development of alternative non-reciprocal technologies compatible with 5G/6G standards and integrated circuit technology [2–5]. Spin-waves offer a promising platform to develop a new class of non-reciprocal devices compatible with integrated circuit technologies thanks to various intrinsic forms of non-reciprocities in frequency [6–8], and amplitude [9–13]. Besides, magnonics enables a scalability down to sub-100 nm sizes[14–19], as well as a tunability in a broad frequency range of the microwave spectrum, making it a field of choice for miniaturizing microwave components [20, 21]. So far, only theoretical efforts have been carried out to study the feasibility of a magnonic circulator, based primarily on numerical simulations of complex architectures. Among these studies, the inverse-design approach requires a magnetic landscape made of submicron squared pixels [22], while another simulation study showing unidirectional coupling schemes relies on complex multilayered geometries including ports on both

sides of the film [23, 24]. While these simulations open new routes for miniaturizing circulators, they require challenging nanoscale dimensions [25], which poses significant challenges for both experimental realization and threshold sensitivity. Consequently, a practical micron-scale experimental demonstration of a circulator remains a critical missing link for integrated magnonic circuits. In this study, we experimentally demonstrate spin-wave circulation at the micron scale on a device based on rectilinear unidirectional spin-wave beams propagating in a thin YIG film. We present results on two different prototypes showcasing genuine spin-wave circulation between three ports, also allowing multi-band operation by engineering the wavevector spectrum directly from the transducer dimensions. By combining this architecture with the frequency selectivity, tunability, and power dependence of spin-waves, we propose a new scheme towards the miniaturization of circulators.

The spin-wave circulator device shown in Fig. 1-(a,b) consists of three pairs of gold nano-bar gratings fabricated on top of a 55 nm-thick Yttrium Iron Garnet (YIG) film grown via liquid phase epitaxy [26]. This design functions as a three rectilinear beam channel architecture covering a total working area of around $100 \times 100 \mu\text{m}^2$. Each grating acts as a chiral transducer, allowing for unidirectional transmission of spin-waves between two ports [11]. The circulation scheme is achieved by translating the pairs of gratings, in order to create three separate channels, through which spin-wave beams propagate rectilinearly from one port to another.

The essence of the non-reciprocity used in our device

* kevin.weber@imt-atlantique.fr

† vincent.vlaminck@imt-atlantique.fr

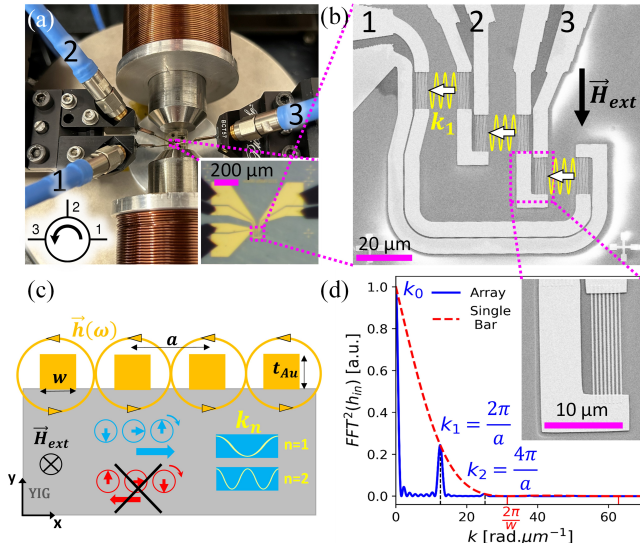


FIG. 1. (a) 3-port spin-wave spectroscopy setup. (inset) Optical microscope image of the circulator prototype. (b) SEM image of the circulator. Arrows indicate the rectilinear spin-wave channels and circulation direction defined by the external field polarity. (c) Schematic of the chiral phase-matching mechanism between the microwave field distribution of the gold nanowires (yellow circles) and the spin-wave phase profiles (blue and red circles). (d) Fourier transform of the excitation field from the grating, showing a comb of wavevector $k_n = n \cdot 2\pi/a$. (inset) High-magnification SEM of the gold nano-bar transducers.

is sketched in Fig. 1-(c). It relies on the chiral excitation of spin-waves in the Damon-Eschbach configuration, which originates from the matching of the distribution of the microwave Oersted fields generated by the nanowire gratings (yellow circles) with the spin-wave phase profile sketched with blue and red circles respectively for right and left propagating waves. As illustrated in Fig. 1-(c), only the waves propagating to the right-hand side of the static magnetization direction \vec{M} will effectively be excited, accordingly with the cross-product rule [13, 27, 28]:

$$\frac{\vec{k}}{\|\vec{k}\|} \times \frac{\vec{M}}{M_s} = \vec{u}_y \quad (1)$$

where \vec{u}_y is the unitary vector pointing out-of-the plane in the direction from the film to the grating. In other words, this unidirectional excitation, and thus the direction of circulation, can be inverted with the polarity of the external bias field \vec{H}_{ext} , or also if the grating is located below the YIG film.

Furthermore, the grating's geometry provides a spectral excitation signature in the form of a comb of wavevector corresponding to integral values of the spatial periodicity a of the nanowires [11, 29], namely $k_n = n \cdot \frac{2\pi}{a}$, $n \in \mathbb{N}_0$, as shown in Fig. 1-(d) with the Fourier transform of the excitation field. This allows for a specific selection of several narrow frequency bands, which can be adjusted

with the grating's dimensions. Both investigated devices share a gold thickness of $t_{Au} = 40$ nm, a nano-bar length of $13 \mu\text{m}$, and array grating width of $4 \mu\text{m}$. The first device shown in the scanning electron microscopy (SEM) image in the inset of Fig. 1-(d) utilizes a nano-bar width $w = 200$ nm, and a periodicity $a = 500$ nm with an inter-transducer distance $d = 15 \mu\text{m}$. The second device, with its corresponding nano-bar displayed in the inset of Fig. 4-(a), features reduced dimensions with $w = 100$ nm, $a = 400$ nm, and a distance of $d = 10 \mu\text{m}$. In the following, we characterize the performance of each device demonstrating the circulation over multi-bands of frequency by engineering the wavevector spectrum with the gratings dimensions.

The devices were characterized by 3-port spin-wave spectroscopy using a Rhode&Schwarz-ZNA43 vector network analyzer [30], and a PM8 probe station shown in Fig. 1-(a) utilizing a combination of EDP-style dual and single picoprobes [31]. The whole setup was calibrated via a three-port SOLT (Short, Open, Load, Through) protocol using a CS-3 differential calibration substrate [32] in order to de-embed the magnonic signal from the rest of the setup. Figure 2-(a) displays the frequency-field map of the real part of S_{12} , S_{23} , S_{31} in linear scale, namely the transmission from port 2 to port 1, port 3 to port 2, and port 1 to port 3, as indicated by the arrows in Fig. 1-(b). Measurements are performed across an external field range from -100 to $+100$ mT with a 2 mT increment, while the frequency was swept from 0.1 to 6 GHz with 1601 steps. For this mapping, we performed single spectral scans without averaging, while applying -15 dBm of input power, and with an intermediate frequency bandwidth (BW_{IF}) of 500 Hz, which resulted in a 66 s acquisition time for each frequency sweep. Owing to the weak inductive coupling, we chose to remove the parasitic baseline by performing a relative measurement of the scattering parameters $\Delta S = S_{meas} - S_{ref}$. The reference spectrum S_{ref} was recorded at an external field $\mu_0 H_{ref} = 200$ mT sufficiently large to displace all spin-wave dynamics outside of the experimental frequency range. Additionally, we show in appendix (Fig. 5-(a)) a typical spectra of the raw data for each port at both low and high bias field, which display different insertion losses between each transmission channel, mainly due to the different crosstalk between the dual and single picoprobes. The transmission spectra on this device reveals two branches corresponding respectively to the first two peaks $k_0 \approx 0$ and $k_1 = \frac{2\pi}{a} \approx 12.6$ rad/ μm , for which we expect the most efficient spin-wave generation to occur from the excitation field's spectral density shown in Fig. 1-(d). The latter branch (k_1) possesses a strong amplitude asymmetry between positive and negative fields, consistently with the cross-product rule of Eq.(1), while the k_0 branch remains largely symmetric. This difference in asymmetry between the k_0 and k_1 branches is expected from a more pronounced circular ellipticity of the excitation field felt by the higher wavevectors, which is a requirement for the chiral coupling [11, 13, 28]. The

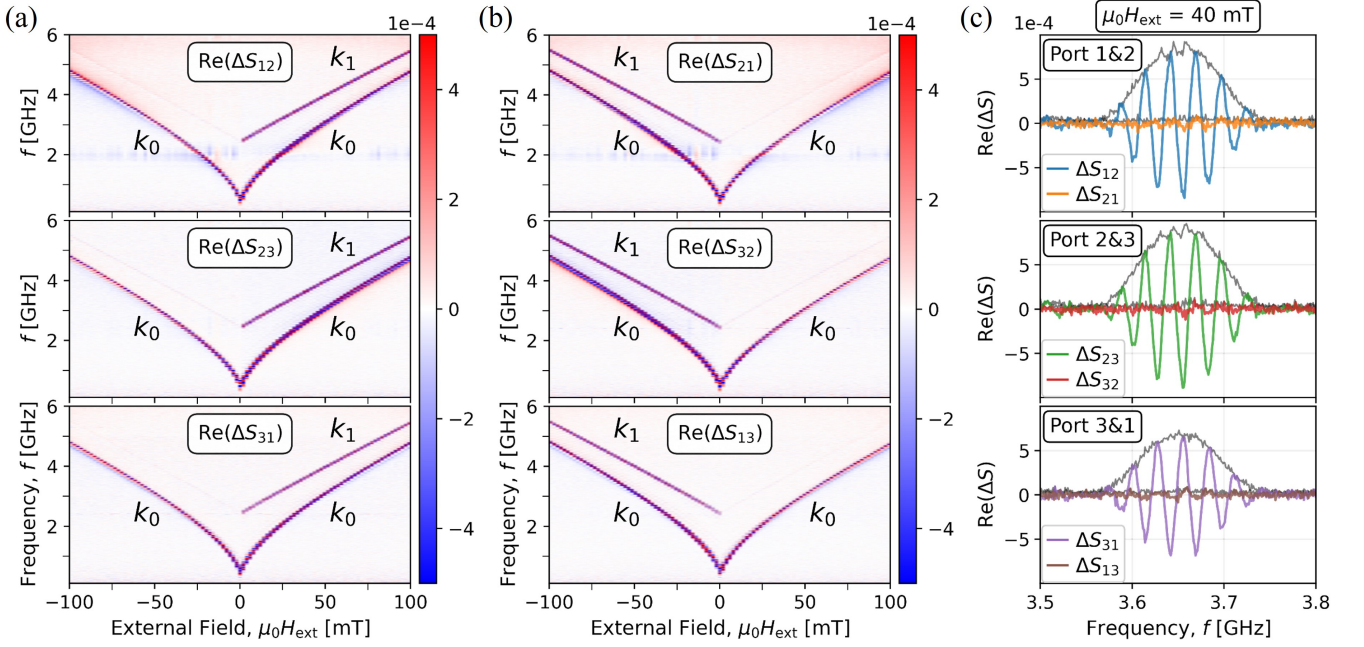


FIG. 2. (a) Frequency-field mappings of the relative scattering parameters ΔS_{ij} for the three circulation channels. The k_1 branch shows clear amplitude asymmetry consistent with chiral excitation. (b) Complementary (f, H_{ext}) maps ΔS_{ji} . (c) (color) Representative transmission spectra $\Delta \text{Re}(S_{ij})$ for $i, j \in \{1, 2, 3\}$ at $\mu_0 H_{\text{ext}} = 40$ mT, and their magnitude (grey). All data were acquired at an input power of -15 dBm using a reference field of $\mu_0 H_{\text{ref}} = 200$ mT.

reciprocal spectra S_{21}, S_{32}, S_{13} shown Fig. 2-(b) displays identical spin-wave features with opposite applied field polarity, consistently with Eq.(1). Additionally, Figure 2-(c) shows typical spectra at $\mu_0 H_{\text{ext}} = 40$ mT of all transmission S-parameters, namely both ΔS_{ij} and ΔS_{ji} for $i, j \in \{1, 2, 3\}$ and $i \neq j$, confirming the unidirectional nature of the beams excited by the grating (see also Appendix Fig. 7 for representative spectra over 400 mT field range). These distinct contrast between passing and isolated ports demonstrates a genuine circulation of spin-waves between all three ports.

By converting our measured 3×3 scattering matrices into impedance matrices (as detailed in Appendix C), we obtain the dynamic inductance spectra ΔL_{ij} . From these, we summarize in Figure 3-(a) the field dependence of the extracted spin-wave propagation properties [33], which includes the group velocity v_g , the attenuation length L_{att} , and the corresponding relaxation time $\tau_r = L_{\text{att}}/v_g$. These characteristics demonstrate that the prototype functions effectively as a combined non-reciprocal circulator and programmable delay line. This field-dependent delay provides a powerful tool to directly investigate spin-wave propagation dynamics. Experimentally, the group velocity was extracted from time-of-flight measurements via $v_g = \frac{d\omega}{dk} = \frac{d}{\tau_{\text{ToF}}}$, where $\tau_{\text{ToF}} = -\frac{d\phi(\omega)}{d\omega}$ and $\phi(\omega)$ is the phase of the transmission spectra. It reveals an identical monotonic decrease across all transmission channels as the bias field increases, from 515 m.s^{-1} at 0 mT to 355 m.s^{-1} at 100 mT, in very good agreement with the theoretically calculated group

velocity (indicated by dashed lines), derived from the dispersion relation [34]:

$$\omega_{\text{res}}^2(k, H) = \Omega_k(\Omega_k + \omega_M) + \omega_M^2 P(1 - P) \quad (2)$$

where $\omega_M = \gamma\mu_0 M_s$, $\Omega_k = \gamma\mu_0 H_{\text{equ}} + \omega_M \Lambda^2 k^2$ with $\Lambda^2 = \frac{2A_x}{\mu_0 M_s^2}$ the exchange length, and $P = 1 - \frac{1-e^{-kt}}{kt}$, which reflects the influence of the dynamic dipolar interaction. To estimate the attenuation length L_{att} , we consider an exponential decay and estimate the ratio of the mutual inductance amplitude to the absorptive part of the self-inductance $|L_{ij}/\text{Im}(L_{jj})| \approx \exp(-\frac{d}{L_{\text{att}}})$ (see also Appendix Fig. 8), where d is the inter-transducer distance. This approach, which effectively de-embeds the local transduction efficiency, shows a mild decrease of L_{att} with the bias field, yielding similar values for the channels 1–2 and 2–3 ranging from $60 \mu\text{m}$ at low fields down to $40 \mu\text{m}$ at 100 mT, while the channel 3–1 exhibits slightly reduced attenuation length ranging from $30 \mu\text{m}$ to $20 \mu\text{m}$ respectively. This slight reduction, which is also visible in the amplitude of the transmission spectra, is likely due to the shape of our prototype which requires a longer termination of port 1 in order to couple with port 3, resulting in additional ohmic loss compared with the two other ports. This minor weakness could be corrected with a proper microwave engineering of the scheme in order to balance all ports. Consequently, the calculated relaxation time remains remarkably stable near 100 ns, (respective 60 ns for L_{13}) across the entire field range. These results demonstrate

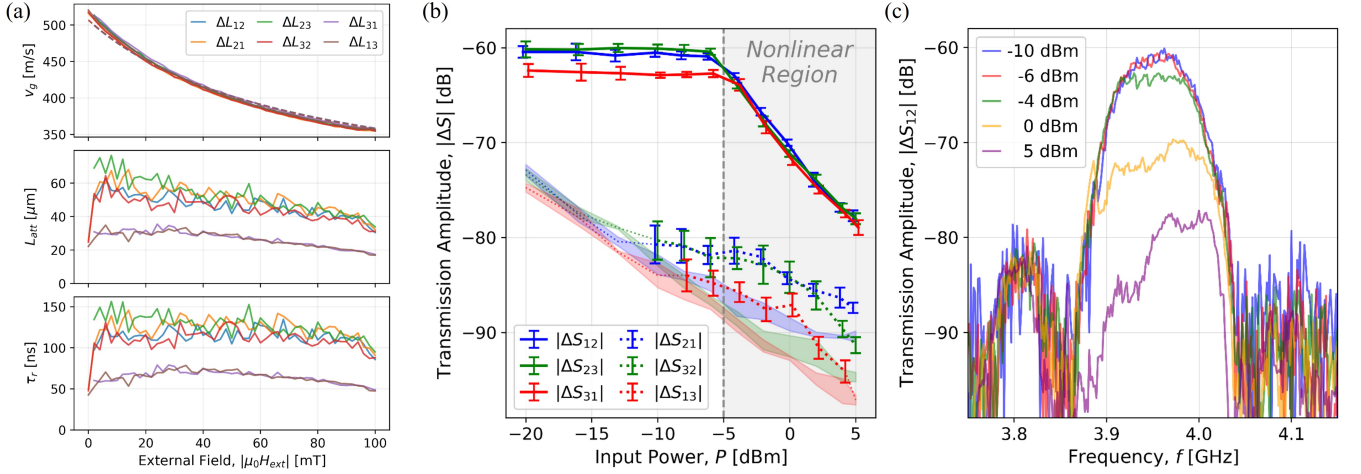


FIG. 3. (a) Bias field dependence of the spin-waves transport properties derived from the inductances ΔL_{ij} (extracted from the data in Fig. 2) in the passing polarity of the bias field. (top) group velocity v_g , where dashed lines represent theoretical calculations based on the dispersion relation Eq.(2), (middle) attenuation length L_{att} , and (bottom) relaxation time $\tau_r = \frac{L_{\text{att}}}{v_g}$. (b) Power dependence of the transmission amplitudes of the k_1 peaks at $\mu_0 H_{\text{ext}} = 50$ mT in the passing (solid line), and isolated (dashed line) direction, including an estimated noise floor level (shaded bands). (c) Spectra comparison showing the spectral distortion and amplitude saturation of ΔS_{12} past the non-linear threshold at -5 dBm. The measurements in (b) and (c) were acquired using a reference field of $\mu_0 H_{\text{ref}} = 300$ mT.

that the chosen inter-transducer distance, $d = 15 \mu\text{m}$, is well within the attenuation length across the entire field range, confirming that the observed insertion loss is not primarily limited by spin-wave decay, but is instead dominated by the poor impedance radiation matching at this length scale [35–37].

The performance and power handling of the circulator were separately investigated for various input powers P_{in} ranging from -20 dBm to 5 dBm, and various bias field up to 200 mT. Figure 3-(b) depicts the power dependence maximum transmission amplitudes for the k_1 branch in both the passing and the blocking directions across all ports at a bias field of $\mu_0 H_{\text{ext}} = 50$ mT. Below $P_{\text{in}} = -6$ dBm, the device behaves linearly with the relative spin-wave transmission magnitude, independent of the input power, pointing around -60 dB. It shows a difference of more than 20 dB between the passing and the blocking directions, with backward signals remaining indistinguishable from the experimental noise floor indicated by the dotted line in the shaded regions. As the power exceeds -6 dBm, the system enters a non-linear regime characterized by spectral distortion and amplitude reduction. These findings are consistent with the non-linear power-limiting effects observed by Davidkova et al.[38], which is due to the onset of multi-magnon scattering processes in YIG thin films. This transition is resolved in Fig. 3-(c), which superimposes the forward transmission spectra $|\Delta S_{12}|$ at varying power levels. While the response remains consistent up to -6 dBm, higher powers induce progressive peak compression and broadening, altering the operation of the circulator. Notably, the non-linear threshold varies slightly with the

bias field, shifting from approximately -5 dBm at 50 mT to -6 dBm at 100 mT, before increasing to -3 dBm at 200 mT (as shown in Appendix Fig. 5). The observed increase in the non-linear threshold qualitatively aligns with established theories on high-power microwave instability [39]. However, because our prototype’s return loss varies across the frequency range, this non-uniform return loss slightly disrupts the expected monotonous increase of the non-linear threshold.

To further explore the limits of frequency selectivity, and the potential for multi-band operation in magnonic circuits, we fabricated a second device with a reduced width $w = 100$ nm, periodicity $a = 400$ nm, and an inter-transducer distance $d = 10 \mu\text{m}$ (refer to inset of Fig. 4-(a)). The discrete wavevectors allowed by the grating periodicity, occurring at $k_n = n \cdot 2\pi/a$, have their relative excitation strength sampled by the single-bar envelope as indicated by the red dashed line in Fig. 4-(a), and whose first zero is located at $2\pi/w \approx 62.8$ rad/ μm . By optimizing the a/w ratio to a value of 4 (an increase from the 2.5 ratio used in our first device), we effectively enhance the excitation strength of this next wavevector $k_2 \approx 31.4$ rad/ μm . Physically, this geometric ratio dictates how many wavevector peaks of the excitation comb fit within the main lobe of the single-bar envelope, thereby increasing the spectral weight at k_2 .

The experimental validation of this multi-wavevector excitation is captured in the frequency-field mapping of the transmission magnitude ΔS_{31} shown in Fig. 4-(b) in a bias field range up to 50 mT. The map clearly resolves three distinct branches: a dominant and sym-

metric $k_0 \approx 0$ branch, alongside then non-reciprocal k_1 and k_2 branches. Additionally, intermediate small ripple structures, also exhibiting similar non reciprocity, are visible between k_0 and k_1 , and correspond to the secondary lobes of the grating's Fourier transform. We show in Figure 4-(c) a typical spectra at $\mu_0 H_{\text{ext}} = 20$ mT for this device zoomed around the peaks corresponding to the wavevector k_1 and k_2 . Despite the inherent increase in insertion losses at higher wavevectors, reaching 67 dB for k_1 and 85 dB for k_2 , both remain non-reciprocal, with a chiral isolation of 23 dB for k_1 and at least 14 dB for k_2 above the noise floor. The residual signal observed in the isolation direction of k_1 is likely attributed to a non-complete chiral coupling, or perhaps a parasitic absorption and re-emission at the intermediate port 2.

Finally, the frequency dependence of the propagation properties, quantified through time of flight measurements τ_{ToF} and group velocity $v_g = d/\tau_{\text{ToF}}$, are shown in Fig. 4-(d). We observe a distinct field-dependent behavior between the two branches. For the k_1 mode, τ_{ToF} increases from 19 ns to 23 ns as the bias field is swept up to 50 mT, corresponding to a group velocity comparable to the one extracted for the first device. In stark contrast, the k_2 branch maintains a remarkably invariant time of flight of $\tau_{\text{ToF}} \approx 16$ ns across the same field range, which results in a constant group velocity of ≈ 635 m.s $^{-1}$ greater than the one for k_1 . This disparity is fundamentally rooted in the underlying dispersion relation Eq.(2). Namely, the influence of the dynamic dipolar term in the dispersion is more pronounced at the lower wavevector k_1 , which makes its curvature more sensitive to the Zeeman shift of the spin-wave manifold. However, at the higher wavevector k_2 , the dispersion enters a regime increasingly dominated by the quadratic exchange term ($\propto k^2$). In this exchange-active region, the dispersion slope becomes less affected by external field variations, resulting in the observed constant group velocity. This transition provides a versatile platform offering different timing characteristics for signal routing in miniaturized microwave architectures, where both field-tunable and field-robust time-delay can be exploited simultaneously.

In summary, we have successfully implemented a comprehensive three-port spin-wave spectroscopy to characterize the circulation of microwave power at a micron-scale. This experimental platform allows for the de-embedding of multi-channel scattering parameters, providing a rigorous verification of non-reciprocal signal routing in integrated magnonic circuits. We showcase a magnonic circulator prototype based on 3 pairs of nano-gratings, acting as a three rectilinear beam channel design operating over a working area of $100 \times 100 \mu\text{m}^2$. This device, a first of its kind, exhibits quasi even level of transmission amplitude, and isolation greater than 20 dB between ports, allowing for a proper microwave circulation. Further engineering of the grating's dimensions enables the excitation of additional higher-order wavevector branches, offering a versatile route for the development of multi-band and frequency-selective

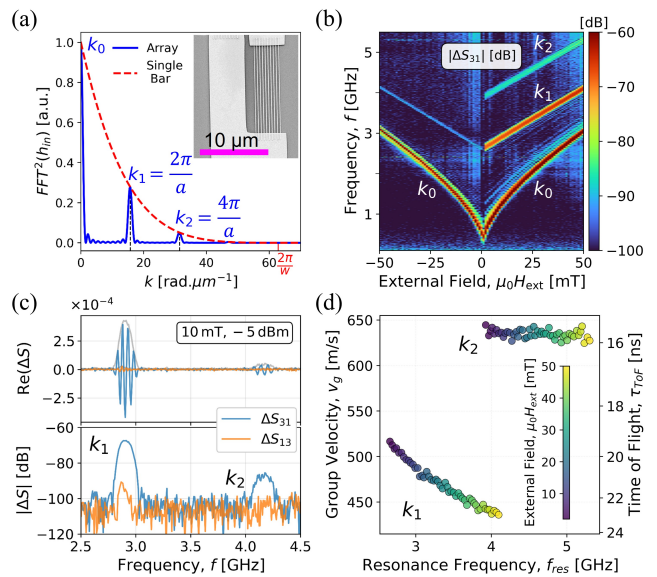


FIG. 4. 2^{nd} device with reduced nano-bar width $w = 100$ nm and periodicity $a = 400$ nm. (a) Fourier transform of the excitation with an inset displaying an SEM image of the reduced nano-bar array. (b) Frequency-field map of ΔS_{31} (acquired using $\mu_0 H_{\text{ref}} = 250$ mT and -5 dBm input power) revealing a second chiral wavevector branch k_2 . (c) Corresponding spectra at 10 mT showing unidirectional transmission for both k_1 and k_2 peaks, (top) real part $\text{Re}(S_{31})$, and (bottom) magnitude $|S_{31}|$. (d) Field dependence of the group velocity v_g and the time of flight τ_{ToF} for both k_1 and k_2 peak.

magnonic components. These findings establish a scalable pathway for the integration of non-reciprocal technologies into high-frequency 5G/6G architectures and cryogenic quantum systems.

ACKNOWLEDGMENTS

This project has received co-funding from the European Union's Horizon Europe Research and Innovation Program under Grant Agreement No. 101126644. It further benefited from a government grant operated by the French National Research Agency as part of the France 2030 program, Reference No. ANR-22-EXSP-0004(SWING), as well as the ANR project MagFunc/ANR-20-CE91-0005. M.L. received funding from the German Bundesministerium für Wirtschaft und Energie (BMWi) under Grant No. 49MF180119. We thank Hicham Majjad, Thibaut Devolder, and Asma Mouhoub for their help with the nanofabrication and Mufti Avicena for meaningful discussions.

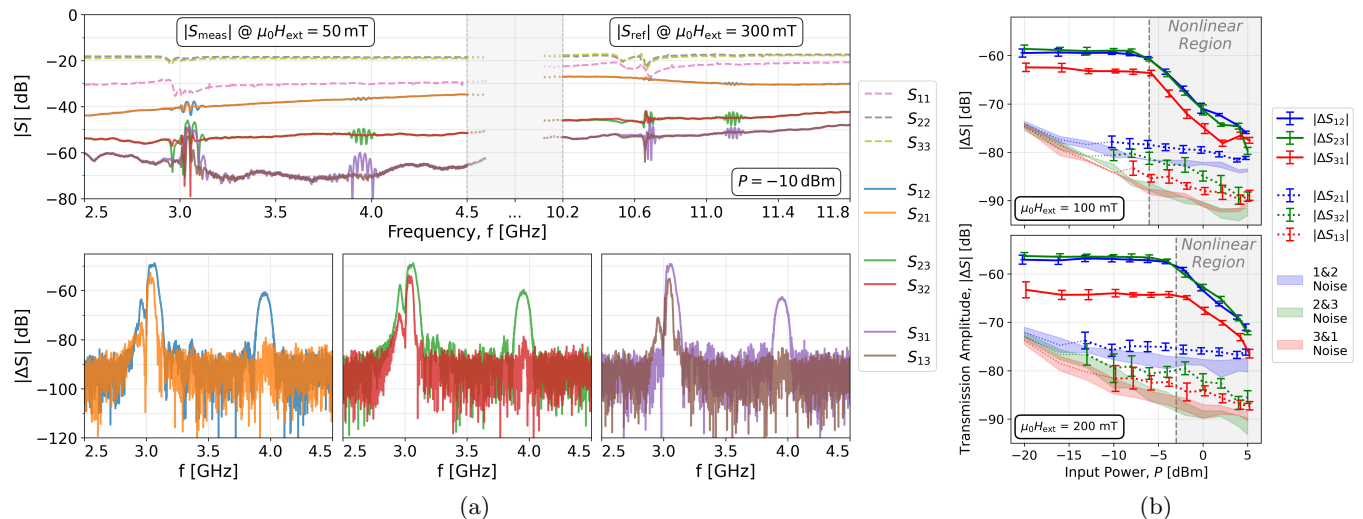


FIG. 5. (a) Raw data with insertion and rejection loss. (b) Power dependence at $\mu_0 H_{ext} = \{100 \text{ mT}, 200 \text{ mT}\}$ at $\mu_0 H_{ref} = 300 \text{ mT}$.

Appendix A: Raw Data and Power

The background-subtraction procedure used to isolate the magnonic signal from electromagnetic (EM) crosstalk is illustrated in Fig. 5-(a). The upper panel displays the raw transmission magnitude $|S_{ij}|$ at $\mu_0 H_{ext} = 50 \text{ mT}$ compared to a reference baseline recorded at $\mu_0 H_{ext} = 300 \text{ mT}$ (input power $P = -10 \text{ dBm}$). These raw spectra reveal that the inductive crosstalk is not uniformly balanced across the device, namely the EM coupling is most pronounced between ports 1 and 2 with a baseline at -40 dB , while the port pair 3–1 exhibits the lowest background levels at -65 dB . This difference in the crosstalk between the dual and single picoprobes is a limitation inherent to the shape of this EDP-style GGB dual-picoprobes, which unfortunately don't allow to tackle small signal below this baseline. The baseline-corrected signals (lower panel), defined as $\Delta S_{ij} = S_{ij}(H) - S_{ij}(H_{ref})$, clearly resolve the underlying magnonic resonances. At this specific power level (-10 dBm), the low- k branch (k_0) is already significantly distorted, indicating operation within the non-linear regime. In contrast, the k_1 peak retains a well-defined Gaussian lineshape and possess high directional contrast, suggesting a higher threshold for non-linear instabilities at larger wavevectors, in accordance with the wavevector dependent excitation efficiency given by the spectral density of the excitation field illustrated in Fig. 1-(d) and Fig. 4-(a). Figure 5-(b) presents the power-dependent analysis for external fields of 100 mT and 200 mT . While the qualitative evolution of the spectra matches the 50 mT data discussed in the main text, the non-linear power threshold—marked by the onset of peak compression and broadening—varies with the bias field. We observe a minor reduction of this threshold to -6 dBm at 100 mT , and an increase to -3 dBm at 200 mT , which is somewhat

consistent with the known 3/4 power law of magnetic instability at high microwave power [39].

Appendix B: Multi-band Circulation and Maps

The comprehensive 3-port characterization of the second investigated device ($w = 100 \text{ nm}$, $a = 400 \text{ nm}$) is shown in the complete set of frequency–field mappings in Figure 6-(a,b), resolving both the k_1 and k_2 branches across all ports. This second data set highlights the reproducibility of the chiral excitation mechanism and demonstrates the feasibility of higher-order wavevector engineering for multi-band magnonic applications.

Appendix C: S-Parameter Conversion and Inductance Spectra

We display in Figure 7 a panel of inductance spectra over the full 400 mT range of bias field. To extract these spectra, the measured 3×3 scattering matrix \mathbf{S} must be transformed into the impedance matrix \mathbf{Z} . For a general multi-port network, this transformation is defined as:

$$\mathbf{Z} = Z_0(\mathbf{I} + \mathbf{S})(\mathbf{I} - \mathbf{S})^{-1}$$

where \mathbf{I} is the 3×3 identity matrix and $Z_0 = 50 \Omega$ is the characteristic impedance of the measurement system. From the resulting impedance matrix, the frequency-dependent inductance is extracted from the imaginary part:

$$L_{ij} = \frac{\text{Im}(Z_{ij})}{2\pi f}$$

Applying the reference field subtraction yields the purely dynamic magnonic inductance $\Delta L_{ij} = L_{ij}(H_{ext}) -$

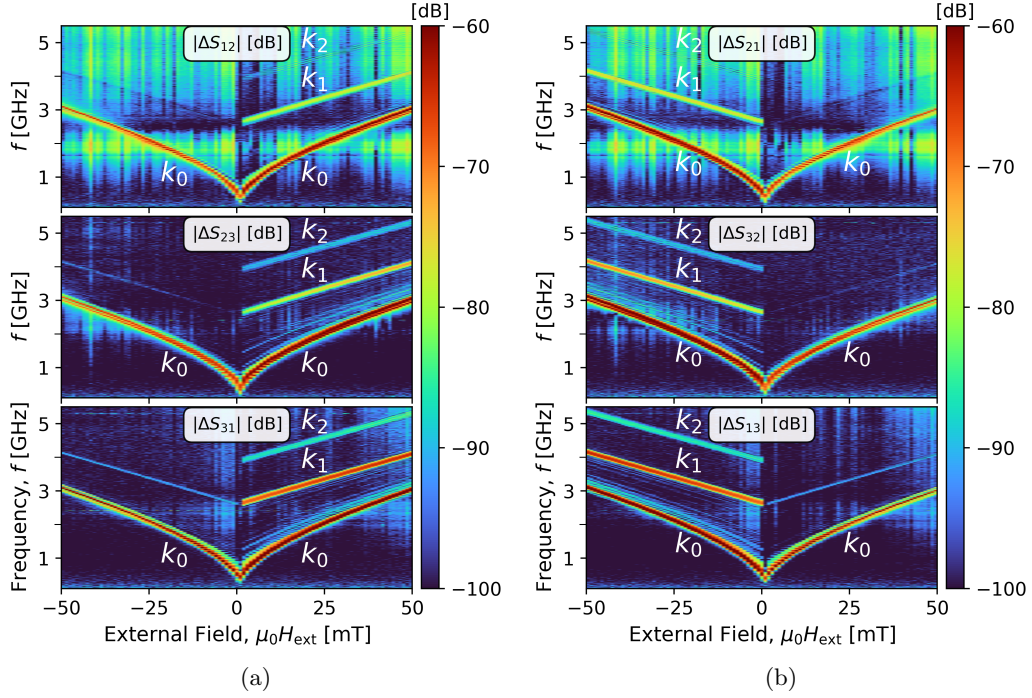


FIG. 6. (a) Full (f, H_{ext}) mapping and (b) complementary transmission maps for the second device. Data were acquired using a reference field of $\mu_0 H_{\text{ref}} = 250$ mT at an input power of -5 dBm.

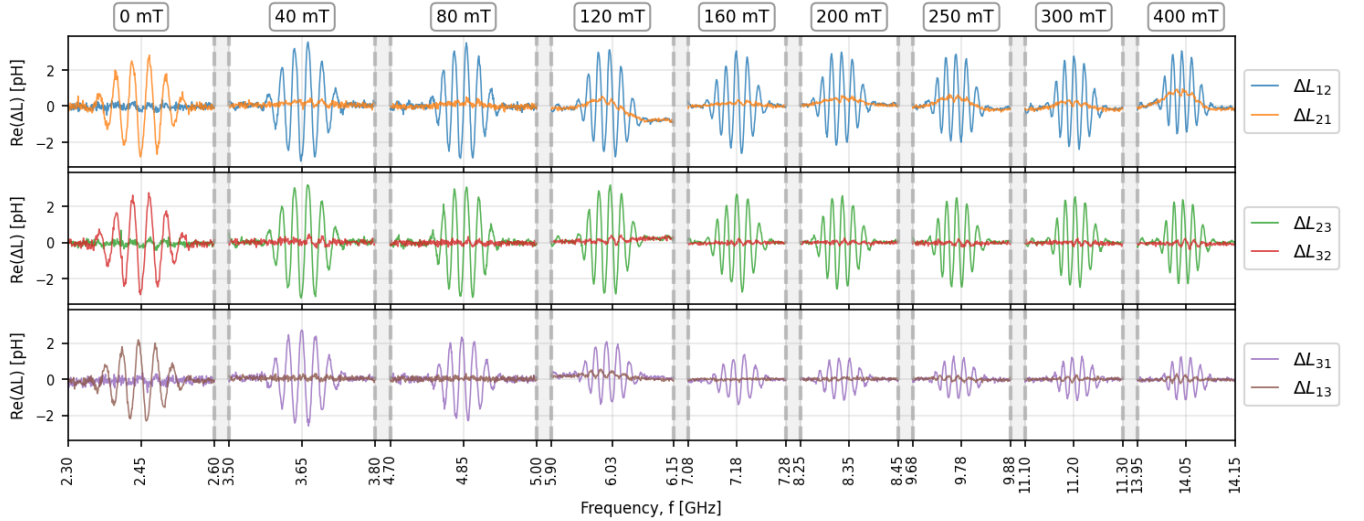


FIG. 7. Example spectra $\Delta L_{ij} = L_{ij}(H_{\text{ext}}) - L_{ij}(H_{\text{ref}})$ of the k_1 branch for the first device, measured at an input power of -10 dBm. Data are shown for external bias fields $\mu_0 H_{\text{ext}} = 0, 40, 80,$ and 120 mT using a reference field of $\mu_0 H_{\text{ref}} = 300$ mT, and for $\mu_0 H_{\text{ext}} = 160, 200, 250, 300,$ and 400 mT using $\mu_0 H_{\text{ref}} = 10$ mT.

$L_{ij}(H_{\text{ref}})$. Figure 7 shows that the amplitude of the spin-wave transmission signal remains fairly constant for the channel 12, and 23, while it decreases slightly for the channel 31.

Appendix D: Inductance Ratio

To further elucidate the extraction of the attenuation length L_{att} , Figure 8 presents the field-dependent evolution of the transmission-to-reflection inductance ratio, $|L_{ij}/\text{Im}(L_{jj})|$. This metric effectively isolates the intrinsic spin-wave propagation dynamics from local transduction efficiencies. As shown, the propagation channels 1–2

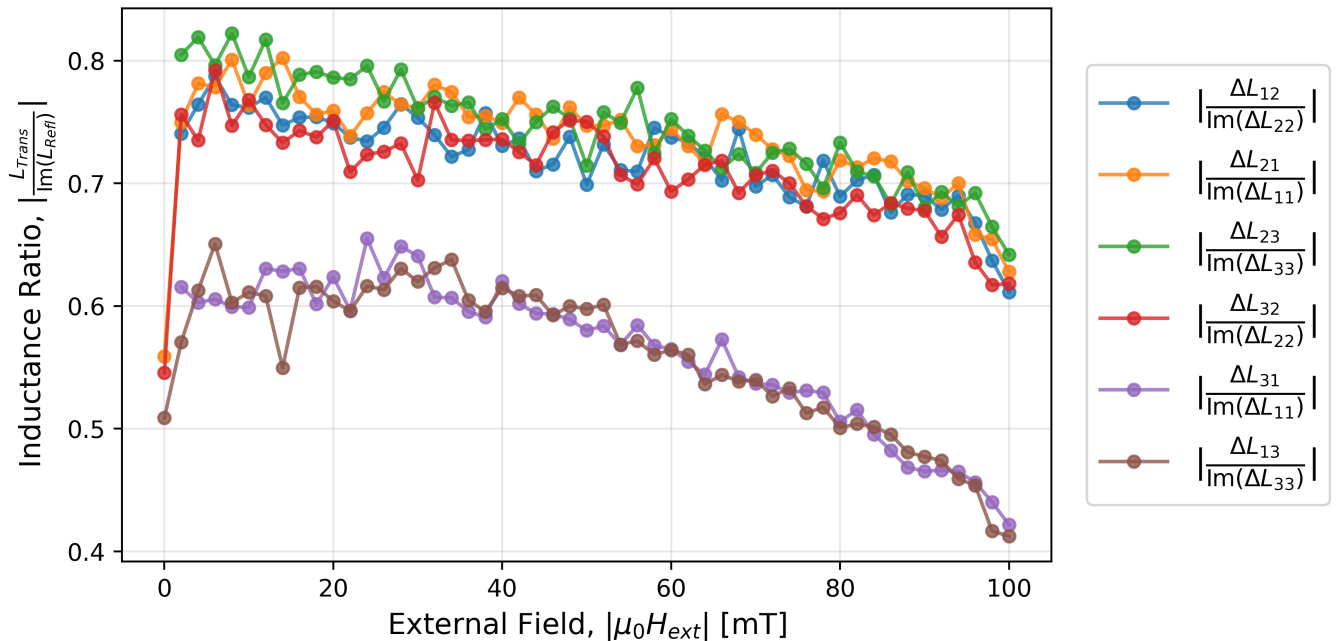


FIG. 8. Inductance amplitude ratios for attenuation length estimation for the first device at. The ratio of the mutual (transmission) inductance amplitude to the absorptive part of the self- (reflection) inductance, $|L_{ij}/\text{Im}(L_{jj})|$, is plotted as a function of the external magnetic field magnitude $|H_{\text{ext}}|$, corresponding to the passing polarity of the bias field for each respective channel.

and 2–3 exhibit highly symmetric behavior, with their inductance ratios mildly decreasing from approximately 0.8 at low fields down to 0.6 at 100 mT. In contrast, channel 3–1 yields systematically lower ratio values, ranging from

roughly 0.6 down to 0.4 over the same field range. This disparity mirrors the slightly reduced attenuation length and lower transmission spectra amplitude observed and discussed for this channel in the main text.

-
- [1] V. G. Harris, Modern microwave ferrites, *IEEE Transactions on Magnetics* **48**, 1075 (2012).
 - [2] H. Lira, Z. Yu, S. Fan, and M. Lipson, Electrically driven nonreciprocity induced by interband photonic transition on a silicon chip, *Physical Review Letters* **109**, 10.1103/PhysRevLett.109.033901 (2012).
 - [3] N. Reiskarimian and H. Krishnaswamy, Magnetic-free non-reciprocity based on staggered commutation, *Nature Communications* **7**, 10.1038/ncomms11217 (2016).
 - [4] A. C. Mahoney, J. I. Colless, S. J. Pauka, J. M. Hornibrook, J. D. Watson, G. C. Gardner, M. J. Manfra, A. C. Doherty, and D. J. Reilly, On-chip microwave quantum hall circulator, *Physical Review X* **7**, 10.1103/PhysRevX.7.011007 (2017).
 - [5] L. Ranzani and J. Aumentado, Circulators at the Quantum Limit: Recent Realizations of Quantum-Limited Superconducting Circulators and Related Approaches, *IEEE Microwave Magazine* **20**, 112 (2019).
 - [6] M. Grassi, M. Geilen, D. Louis, M. Mohseni, T. Brächer, M. Hehn, D. Stoeffler, M. Bailleul, P. Pirro, and Y. Henry, Slow-Wave-based nanomagnonic diode, *Physical Review Applied* **14**, 10.1103/PhysRevApplied.14.024047 (2020).
 - [7] M. Haidar, M. Bailleul, M. Kostylev, and Y. Lao, Nonreciprocal oersted field contribution to the current-induced frequency shift of magnetostatic surface waves, *Physical Review B* **89** (2014).
 - [8] O. Gladii, M. Haidar, Y. Henry, M. Kostylev, and M. Bailleul, Frequency nonreciprocity of surface spin wave in permalloy thin films, *Physical Review B* **93**, 10.1103/physrevb.93.054430 (2016).
 - [9] J. Chen, T. Yu, C. Liu, T. Liu, M. Madami, K. Shen, J. Zhang, S. Tu, M. S. Alam, K. Xia, M. Wu, G. Gubbiotti, Y. M. Blanter, G. E. W. Bauer, and H. Yu, Excitation of unidirectional exchange spin waves by a nanoscale magnetic grating, *Physical Review B* **100**, 10.1103/physrevb.100.104427 (2019).
 - [10] L. Temdie, V. Castel, C. Dubs, G. Pradhan, J. Solano, H. Majjad, R. Bernard, Y. Henry, M. Bailleul, and V. Vlamincq, High wave vector non-reciprocal spin wave beams, *AIP Advances* **13**, 10.1063/9.0000535 (2023).
 - [11] L. Temdie, V. Castel, T. Reimann, M. Lindner, C. Dubs, G. Pradhan, J. Solano, R. Bernard, H. Majjad, Y. Henry, M. Bailleul, and V. Vlamincq, Chiral Excitation of Exchange Spin Waves Using Gold Nanowire Grating, *Magnetochemistry* **9**, 10.3390/magnetochemistry9080199 (2023).

- [12] T. Devolder, Propagating-spin-wave spectroscopy using inductive antennas: Conditions for unidirectional energy flow, *Physical Review Applied* **20**, 10.1103/physrevapplied.20.054057 (2023).
- [13] D. Wagle, D. Stoeffler, L. Temdie, M. T. Kaffash, V. Castel, H. Majjad, R. Bernard, Y. Henry, M. Bailleul, M. B. Jungfleisch, and V. Vlaminck, Shaping nonreciprocal caustic spin-wave beams, *Physical Review B* **113**, L060405 (2026).
- [14] V. Sluka, T. Schneider, R. A. Gallardo, A. Kákay, M. Weigand, T. Warnatz, R. Mattheis, A. Roldán-Molina, P. Landeros, V. Tiberkevich, A. Slavin, G. Schütz, A. Erbe, A. Deac, J. Lindner, J. Raabe, J. Fassbender, and S. Wintz, Emission and propagation of 1d and 2d spin waves with nanoscale wavelengths in anisotropic spin textures, *Nature Nanotechnology* **14**, 328–333 (2019).
- [15] B. Heinz, T. Brächer, M. Schneider, Q. Wang, B. Lägél, A. M. Friedel, D. Breitbach, S. Steinert, T. Meyer, M. Kewenig, C. Dubs, P. Pirro, and A. V. Chumak, Propagation of spin-wave packets in individual nanosized yttrium iron garnet magnonic conduits, *Nano Letters* **20**, 4220–4227 (2020).
- [16] L. Temdie, V. Castel, M. Jungfleisch, R. Bernard, H. Majjad, D. Stoeffler, Y. Henry, M. Bailleul, and V. Vlaminck, Probing spin wave diffraction patterns of curved antennas, *Phys. Rev. Appl.* **21**, 014032 (2024).
- [17] J. Krčma, O. Wojewoda, M. Hrtoň, J. Holobrádek, J. A. Arregi, J. Panda, E. Pribytova, and M. Urbánek, Mie-enhanced microfocused brillouin light scattering for full wave vector resolution of nanoscale spin waves, *Science Advances* **11**, 10.1126/sciadv.ady8833 (2025).
- [18] V. V. Kruglyak, Chiral magnonic resonators: Rediscovering the basic magnetic chirality in magnonics, *Applied Physics Letters* **119**, 10.1063/5.0068820 (2021).
- [19] J. A. Otálora, M. Yan, H. Schultheiss, R. Hertel, and A. Kákay, Curvature-Induced Asymmetric Spin-Wave Dispersion, *Physical Review Letters* **117**, 10.1103/PhysRevLett.117.227203 (2016).
- [20] B. Dieny, I. L. Prejbeanu, K. Garello, P. Gambardella, P. Freitas, R. Lehdorff, W. Raberg, U. Ebels, S. O. Demokritov, J. Akerman, A. Deac, P. Pirro, C. Adelman, A. Anane, A. V. Chumak, A. Hirohata, S. Mangin, S. O. Valenzuela, M. C. Onbaşlı, M. d’Aquino, G. Prenat, G. Finocchio, L. Lopez-Diaz, R. Chantrell, O. Chubykalo-Fesenko, and P. Bortolotti, Opportunities and challenges for spintronics in the microelectronics industry, *Nature Electronics* **3**, 446–459 (2020).
- [21] A. Barman, G. Gubbiotti, S. Ladak, A. O. Adeyeye, M. Krawczyk, J. Grafe, C. Adelman, S. Cotozana, A. Naeemi, V. I. Vasyuchka, B. Hillebrands, S. A. Nikitov, H. Yu, D. Grundler, A. V. Sadovnikov, A. A. Grachev, S. E. Sheshukova, J. Y. Duquesne, M. Marangolo, G. Csaba, W. Porod, V. E. Demidov, S. Urazhdin, S. O. Demokritov, E. Albisetti, D. Petti, R. Bertacco, H. Schultheiss, V. V. Kruglyak, V. D. Poimanov, S. Sahoo, J. Sinha, H. Yang, M. Münzenberg, T. Moriyama, S. Mizukami, P. Landeros, R. A. Gallardo, G. Carlotti, J. V. Kim, R. L. Stamps, R. E. Camley, B. Rana, Y. Otani, W. Yu, T. Yu, G. E. Bauer, C. Back, G. S. Uhrig, O. V. Dobrovolskiy, B. Budinska, H. Qin, S. Van Dijken, A. V. Chumak, A. Khitun, D. E. Nikonov, I. A. Young, B. W. Zingsem, and M. Winklhofer, The 2021 Magnonics Roadmap (2021).
- [22] Q. Wang, A. V. Chumak, and P. Pirro, Inverse-design magnonic devices, *Nature Communications* **12**, 10.1038/s41467-021-22897-4 (2021).
- [23] K. Szulc, P. Graczyk, M. Mruczkiewicz, G. Gubbiotti, and M. Krawczyk, Spin-wave diode and circulator based on unidirectional coupling, *Physical Review Applied* **14**, 10.1103/PhysRevApplied.14.034063 (2020).
- [24] J. Lan, W. Yu, R. Wu, and J. Xiao, Spin-Wave Diode, *Physical Review X* **5**, 10.1103/PhysRevX.5.041049 (2015).
- [25] J. Zhao, L. Feng, M. Ma, and F. Ma, Three-terminal magnonic demultiplexer, power divider, and circulator, *Journal of Magnetism and Magnetic Materials* **586**, 10.1016/j.jmmm.2023.171161 (2023).
- [26] C. Dubs, O. Surzhenko, R. Thomas, J. Osten, T. Schneider, K. Lenz, J. Grenzer, R. Hübner, and E. Wendler, Low damping and microstructural perfection of sub-40nm-thin yttrium iron garnet films grown by liquid phase epitaxy, *Physical Review Materials* **4**, 10.1103/physrevmaterials.4.024416 (2020).
- [27] M. Kostylev, Non-reciprocity of dipole-exchange spin waves in thin ferromagnetic films, *Journal of Applied Physics* **113** (2013).
- [28] T. Yu and G. E. W. Bauer, Chiral Coupling to Magnetodipolar Radiation, in *Chirality, Magnetism and Magnetolectricity: Separate Phenomena and Joint Effects in Metamaterial Structures*, edited by E. Kamenetskii (Springer International Publishing, Cham, 2021) pp. 1–23.
- [29] H. Yu, G. Duerr, R. Huber, M. Bahr, T. Schwarze, F. Brandl, and D. Grundler, Omnidirectional spin-wave nanograting coupler, *Nature Communications* **4**, 10.1038/ncomms3702 (2013).
- [30] Rohde & Schwarz, ZNA Vector Network Analyzers, https://www.rohde-schwarz.com/products/test-and-measurement/vnas/rs-zna-vector-network-analyzers_63493-551810.html (2026), accessed April 28, 2026.
- [31] GGB Industries, PICOPROBE Dual/Differential Microwave Probe, <https://ggb.com/products/dual-differential-microwave-probe/> (2026), accessed April 28, 2026.
- [32] GGB Industries, Differential Calibration Substrates, <https://ggb.com/products/differential-calibration-substrates/> (2026), accessed April 28, 2026.
- [33] N. Loayza, M. B. Jungfleisch, A. Hoffmann, M. Bailleul, and V. Vlaminck, Fresnel diffraction of spin waves, *Phys. Rev. B* **98**, 144430 (2018).
- [34] B. A. Kalinikos and A. N. Slavin, Theory of dipole-exchange spin wave spectrum for ferromagnetic films with mixed exchange boundary conditions, *Journal of Physics C: Solid State Physics* **19**, 7013 (1986).
- [35] D. A. Connelly, G. Csaba, H. R. O. Aquino, G. H. Bernstein, A. Orlov, W. Porod, and J. Chisum, Efficient electromagnetic transducers for spin-wave devices, *Sci. Rep.* **11**, 18378 (2021).
- [36] F. Vanderveken, V. Tyberkevych, G. Talmelli, B. Sorée, F. Ciubotaru, and C. Adelman, Lumped circuit model for inductive antenna spin-wave transducers, *Sci. Rep.* **12**, 3796 (2022).
- [37] F. Bruckner, K. Davídková, C. Abert, A. Chumak, and D. Suess, Micromagnetic simulation and optimization of spin-wave transducers, *Scientific Reports* **15**,

- 10.1038/s41598-025-05463-6 (2025).
- [38] K. Davidkova, K. Levchenko, F. Bruckner, R. Verba, F. Majcen, Q. Wang, M. Lindner, C. Dubs, V. Vlaminck, J. Klíma, M. Urbánek, D. Suess, and A. Chumak, Nanoscale spin-wave frequency-selective limiter for 5G technology, *Physical Review Applied* **23**, 10.1103/PhysRevApplied.23.034026 (2025).
- [39] P. W. Anderson and H. Suhl, Instability in the motion of ferromagnets at high microwave power levels, *Phys. Rev.* **100**, 1788 (1955).